ISSN 1063-7834, Physics of the Solid State, 2018, Vol. 60, No. 2, pp. 382–389. © Pleiades Publishing, Ltd., 2018.
Original Russian Text © A.S. Kamzin, A.A. Valiullin, H. Khurshid, Z. Nemati, H. Srikanth, M.H. Phan, 2018, published in Fizika Tverdogo Tela, 2018, Vol. 60, No. 2, pp. 375–382.

LOW-DIMENSIONAL SYSTEMS

Mössbauer Studies of Core–Shell FeO/Fe_3O_4 Nanoparticles

A. S. Kamzin[a, *], A. A. Valiullin[b], H. Khurshid[c], Z. Nemati[c], H. Srikanth[c], and M. H. Phan[c]

[a] *Ioffe Institute, Politekhnicheskaya ul. 26, St. Petersburg, 194021 Russia*

[b] *Kazan Federal University, ul. Kremlevskaya 18, Kazan, 420008 Tatarstan, Russia*

[c] *Department of Physics, University of South Florida, 4202 E. Fowler Avenue, Tampa, FL 33620, United States*

**e-mail: Kamzin@mail.ioffe.ru*

Received June 26, 2017

Abstract—FeO/Fe_3O_4 nanoparticles were synthesized by thermal decomposition. Electron microscopy revealed that these nanoparticles were of the core–shell type and had a spherical shape with an average size of ~20 nm. It was found that the obtained FeO/Fe_3O_4 nanoparticles had exchange coupling. The effect of anisotropy on the efficiency of heating (hyperthermic effect) of FeO/Fe_3O_4 nanoparticles by an external alternating magnetic field was examined. The specific absorption rate (SAR) of the studied nanoparticles was 135 W/g in the experiment with an external alternating magnetic field with a strength of 600 Oe and a frequency of 310 kHz. These data led to an important insight: the saturation magnetization is not the only factor governing the SAR, and the efficiency of heating of magnetic FeO/Fe_3O_4 nanoparticles may be increased by enhancing the effective anisotropy. Mössbauer spectroscopy of the phase composition of the synthesized nanoparticles clearly revealed the simultaneous presence of three phases: magnetite Fe_3O_4, maghemite γ-Fe_2O_3, and wustite FeO.

DOI: 10.1134/S1063783418020129

1. INTRODUCTION

Magnetic nanoparticles (MNPs) of iron oxides (such as magnetite Fe_3O_4, maghemite γ-Fe_2O_3, and wustite Fe_xO) with their combination of magnetic properties and nanoscale and surface effects are of fundamental scientific and practical importance. MNPs have a variety of promising applications (including biomedical ones): they may be used as contrast amplifiers in magnetic resonance imaging [1], for magnetic hyperthermic therapy of malignant tumors [1–4], and for targeted drug delivery [5]. However, the magnetic properties of the mentioned MNPs are not entirely suitable for biomedical applications. The issue of fabrication of MNPs with the heating process stopping automatically at a temperature of 42–43°C is among those that need to be resolved. The basic limitation consists in the relatively low capacity of known MNPs for heating or their low specific absorption rate (SAR). Higher SAR values are needed in order to enhance the available hyperthermia treatment procedures and address the risks associated with elevated concentrations of MNPs used in such procedures. It was found that the SAR value is affected by several parameters, including the MNP size, the saturation magnetization, and the effective anisotropy [6–8]. The dependence of SAR on the saturation magnetization is linear for macroscopic particles; however, at the nanoscale, the saturation magnetization decreases together with the SAR. Although the problem of increasing the SAR value in nanosized magnetic systems is a challenging one, several promising approaches have been outlined. It was found in [9] that a change in the MNP morphology (surface anisotropy) may result in enhancement of the magnetic response of iron-oxide MNPs if these nanoparticles are shaped in a certain way. It was also reported in [10] that the effective anisotropy in core–shell MNPs may be enhanced by exchange coupling that amplifies the magnetic response and, consequently, intensifies the hyperthermic effect.

The FeO/Fe_3O_4 system with a wustite (FeO) core and a magnetite (Fe_3O_4) shell holds promise for such studies. Fe_xO has the structure of imperfect rock salt with an ordered distribution of iron vacancies. Fe_xO may be oxidized to magnetite and, further, to maghemite γ-Fe_2O_3. The metastability of nanoscale Fe_xO allows one to produce mixed iron-oxide (magnetite, maghemite, wustite) phases. All the three mentioned compounds are based on the approximately face-centered cubic structure of oxygen. Wustite (Fe_xO) is paramagnetic at room temperature and becomes antiferromagnetic or weakly ferrimagnetic (FM) at temperatures below the Néel point $T_N \simeq 190$ K (see, e.g., [11] and references therein). The transition is associated strongly with the imperfection of wustite. Magnetite (Fe_3O_4) has the inverse cubic

spinel structure at room temperature and is ordered ferrimagnetically at temperatures below the Curie point $T_C \approx 860$ K. Nonstoichiometry in all three phases, which have different properties, is observed in this system. They may manifest magnetic exchange interaction that is induced by interfaces between antiferromagnetic Fe_xO and ferromagnetic Fe_3O_4 and results in the hysteresis shift and the coercivity enhancement (see [12] and references therein). In addition, the properties of these multiphase nanoparticles may be affected by the structures of interfaces between phases [13].

The use of $Fe_{1-x}O$ and its subsequent air oxidation provided an opportunity to study the exchange coupling in nanoparticles with FeO cores and shells made of other isostructural FM oxides (e.g., $CoFe_2O_4$, Fe_3O_4, or γ-Fe_2O_3) [14–18]. Although chemical transformations of $Fe_{1-x}O$, $Fe_{1-x}O/Fe_{3-\delta}O_4$, and $Fe_{2-\delta}O_4$ nanoparticles have been investigated extensively (see [14] and references therein), their anomalous magnetic properties, such as the reduced (compared to bulk values) saturation magnetization, exchange bias in single-phase nanoparticles, or high-field susceptibilities, are still poorly understood and are often attributed to a skewed spin structure or defects on the outer surface of particles [19, 20]. This is the reason why studies focused on the relationship between structural features (e.g., defects) inside MNPs and the observed anomalous magnetic properties are needed. It was demonstrated in [21] that the presence of dislocations and twin boundaries in MNPs results in a large discrepancy between the magnetic and the geometric size distributions, while it was noted in [22] that magnetic disordering in MNPs is induced by high strains in the particle core.

The aim of the present study is to synthesize and examine the properties of core–shell (C/S) FeO/Fe_3O_4 MNPs. The obtained results are compared to the already available data for spherical and cubic C/S FeO/Fe_3O_4 MNPs [6, 10, 15, 16, 20, 23–25]. It is demonstrated that spherical C/S FeO/Fe_3O_4 MNPs have a higher magnetization than cubic ones, but their effective anisotropy (both the shape anisotropy and the exchange anisotropy) and SAR values are lower. It is assumed that higher saturation magnetizations lead to into higher SAR values, but the obtained results reveal an alternative way of enhancing the SAR by altering the effective anisotropy of C/S MNPs.

2. EXPERIMENTAL

Core–shell FeO/Fe_3O_4 MNPs were synthesized by nonhydrolytic thermal decomposition of iron(III) acetylacetonate [26]. Thermally unstable iron(III) acetylacetonate starts decomposing at a temperature of approximately 100–105°C with the production of carbon dioxide and acetone [27]. Oleic acid (OA) and oleylamine (OY) (and similar long-chain carboxylic acids and primary amines) were used to stabilize MNPs in a solution. Iron(III) acetylacetonate (0.75 mmol) was dissolved in octadecene (20 mL) mixed with OA (5 mmol) and OY (5 mmol). The mixture was treated with argon heated to ~100°C in order to remove dissolved free oxygen. The temperature was then raised to 200°C, and the mixture was held at this temperature for 1 h. A change in color (from deep red to black) was the indicator of decomposition of iron(III). At the next stage, the mixture was heated additionally to 300°C at a rate of 10°C/min and left to boil with a reflux condenser at 300°C for 1 h. The heat supply was then cut, and the mixture cooled. The system was flushed with a gas mixture (Ar + 5%H_2) throughout the entire reaction process. The system was opened by adding an excess amount of ethanol with subsequent centrifugation and precipitation of a black powder. The fluid above the precipitate (supernatant) was removed, and the dry powder residue was dispersed in hexane.

The crystal structure of the synthesized MNPs was analyzed with a Bruker AXS D8 X-ray diffractometer. A FEI Morgagni 268 60 kW transmission electron microscope (TEM) was used to characterize the size and the shape of MNPs. The magnetic parameters of powder samples were measured using a Quantum Design setup with a vibrating-sample magnetometer (VSM). Temperature dependences of the saturation magnetization (in the range of 10–350 K) were obtained upon cooling both in zero-field conditions (ZFC) and in an external magnetic field (FC) with a strength of 50 Oe. Hysteresis loops (M–H) were measured at 50 and 300 K in an external field with a strength as high as 50 kOe. The transverse susceptibility (TS) was examined with a laboratory-made probe in the temperature range of 50–300 K in a constant magnetic field with a strength as high as 20 kOe and in a field with a strength of 5 Oe and a frequency of 10 MHz. A suspension of MNPs in water with a density of 1 mg/mL and a suspension prepared from a 2% solution of MNPs in agar were used to study the magnetic hyperthermia. An Ambrell Easyheat LI 3542 (4.2 kW) system was used to measure the hyperthermic heating of MNPs. The frequency remained constant (310 kHz), while the magnetic field strength was varied from 400 to 800 Oe.

The identification of wustite FeO, hematite α-Fe_2O_3, magnetite Fe_3O_4, and maghemite γ-Fe_2O_3 phases is one of the key difficulties arising in the process of examination of iron-oxide articles. Wustite and hematite have a cubic crystal structure and a corundum structure, respectively, while magnetite and maghemite have a spinel structure. This is the reason why they are indistinguishable if studied using X-ray techniques. However, the parameters of hyperfine interaction in Mössbauer spectra (MS) of magnetite and maghemite differ greatly, and Mössbauer spectroscopy thus provides a solution to the important

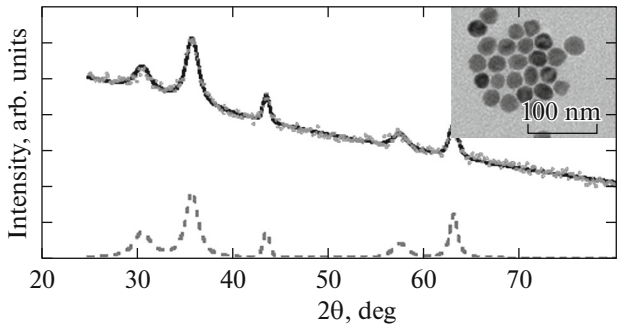

Fig. 1. X-ray diffraction data for spherical FeO/Fe_3O_4 MNPs and the results of mathematical fitting involving the FeO and Fe_3O_4 phases. The TEM image of FeO/Fe_3O_4 MNPs is shown in the inset.

problem of phase analysis in the nanotechnology of magnetic materials. Therefore, Mössbauer spectroscopy with ^{57}Fe and the detection of gamma radiation in the transmission geometry was used to study the magnetic structure and the phase state of the synthesized C/S FeO/Fe_3O_4 MNPs. The reference signal in the system of motion of the Doppler modulator in the spectrometer had a triangular shape needed to set a velocity with a constant acceleration. Co^{57}(Rd) with an activity of 20 mCi was the Mössbauer source of γ-quanta. The velocity scale was calibrated with a 6-μm-thick α-iron foil at room temperature, and a laser interferometer was used for better calibration accuracy. The MS of the studied C/S FeO/Fe_3O_4 MNPs were measured at room temperature. The MOSFIT code [28] was used for mathematical processing of the obtained MS. The hyperfine interaction parameters are denoted as follows: *IS* is the isomer shift (mm/s), *QS* is the quadrupole splitting (mm/s), and H_{eff} is the effective magnetic field (T). The widths of spectral lines are denoted as Γ (mm/s), and % is the percentage of components. The range of theoretical values of hyperfine interaction parameters was determined based on the statistical deviations provided by MOSFIT [28].

3. RESULTS AND DISCUSSION

Figure 1 presents the X-ray diffraction patterns of spherical C/S FeO/Fe_3O_4 MNPs. It follows from the results of analysis of these patterns with the XFIT code [29] that intense lines correspond to the magnetite structure, while weaker lines in the region of ~36° and ~42° correspond to FeO. The TEM image of MNPs is shown in the inset in Fig. 1. It can be seen that the obtained C/S FeO/Fe_3O_4 MNPs are indeed spherical and have the core–shell structure. The average size of C/S FeO/Fe_3O_4 MNPs estimated based on their calculated size distribution is 20 ± 2 nm.

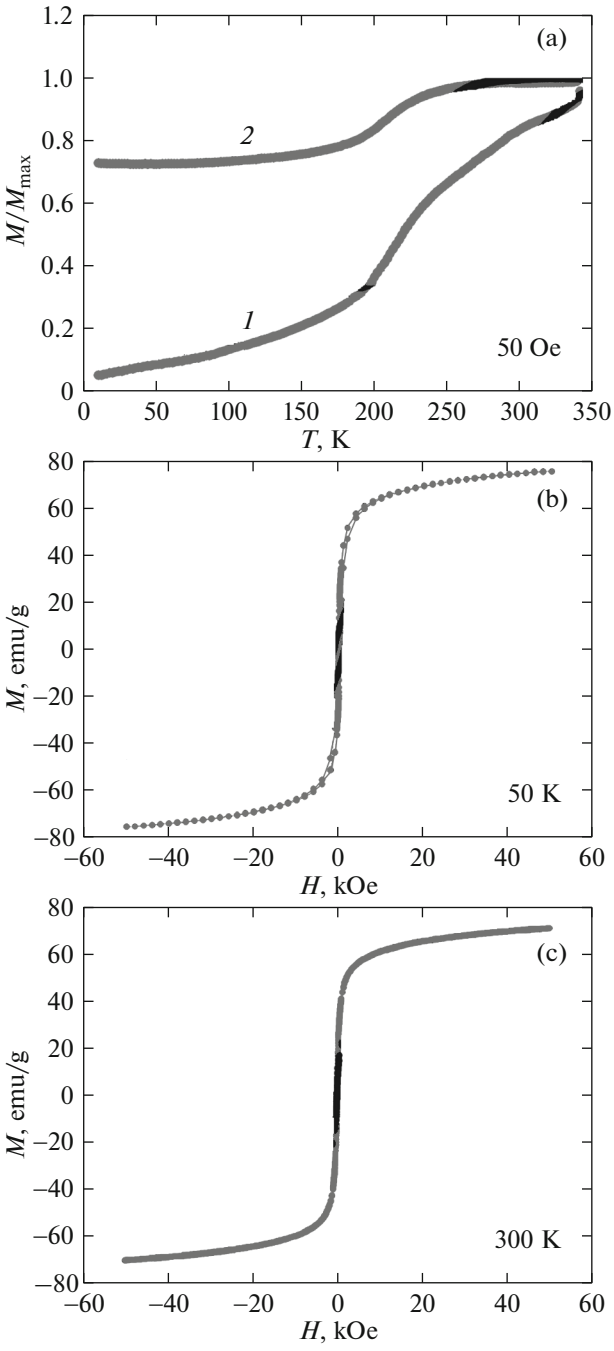

Fig. 2. (a) ZFC (*1*) and FC (*2*) dependences for spherical FeO/Fe_3O_4 MNPs measured in an external field with a strength of 50 Oe. (b, c) Hysteresis loops measured at (b) 50 and (c) 300 K.

Figure 2a shows the *M*–*T* dependences of spherical MNPs measured at 50 Oe in the ZFC and FC regimes. It may be noted that the magnetic behavior of spherical FeO/Fe_3O_4 MNPs is similar to that of other systems of the same kind [6, 16, 26]. The magnetization of particles increases in the process of heating within the studied temperature interval, and the *M*–*T* curve

maximum under ZFC conditions is observed at $T >$ 350 K. This suggests that FeO/Fe_3O_4 MNPs are in the blocked state in the studied temperature range. The FC $M–T$ curve remains almost unchanged below the Néel temperature (T_N), which may be attributed to the existence of a collective spin glass state at low temperatures [30].

Figure 2b shows the $M–H$ hysteresis loops of spherical MNPs measured at 50 and 300 K. The saturation magnetization (M_S) of spherical FeO/Fe_3O_4 MNPs is ~71–75 emu/g. It may be noted that spherical FeO/Fe_3O_4 MNPs have higher M_S values than cubic MNPs [6], but their coercivity (H_C) is lower (Table 1). This difference in M_S values is attributed to the fact that cubic FeO/Fe_3O_4 MNPs have a higher fraction of the FeO phase, and the saturation magnetization in FeO (<20 emu/g) is lower than that in Fe_3O_4 (80–100 emu/g) [6, 15]. The reason for the H_C being lower in spherical MNPs is the same. The difference in coercivity is especially large at low temperatures, since the intensity of the induced anisotropic effect and the H_C value increase with the area of the interlayer between FeO and Fe_3O_4. This is confirmed by the horizontal shift of the hysteresis loop of cubic MNPs cooled to 15 K in an external magnetic field with a strength of 50 kOe (the so-called exchange bias effect, HEB ~ 950 Oe) [6].

A high-precision generator was used to estimate quantitatively the influence of effective anisotropy on particle heating in the context of magnetic hyperthermia [6, 16]. A sample is introduced in such experiments into an induction RF coil that produces an alternating magnetic field with an amplitude no higher than 5 Oe. This field disturbs the sample magnetization. The change in the resonance frequency of the circuit under the influence of an external constant magnetic field may be related directly to the susceptibility of the sample through the inductance. The relative TS change is written as [6]

$$\frac{\Delta\chi_T}{\chi_T}(\%) = \frac{\chi_T(H_{\max}) - \chi_T(H)}{\chi_T(H_{\max})} \times 100, \qquad (1)$$

where $H_{\max}$ is the maximum applied constant magnetic field. The TS dependences obtained at 300 and 50 K by field scanning are shown in Fig. 3. Two lines corresponding to the effective anisotropy fields ($\pm H_A$) are seen; these lines are broadened by the particle size distribution and the anisotropy fields distribution. At 300 K, the TS maximum is located at ~295 Oe. The H_A value increases at low temperatures and is as high as 745 Oe at 50 K for spherical FeO/Fe_3O_4 MNPs. In addition, the amplitude ($\Delta\chi/\Delta\chi_{\max}$) of the line of spherical FeO/Fe_3O_4 MNPs is much higher than that of cubic MNPs [6], which may be attributed to an excess amount of FeO in spherical MNPs. At temperatures close to those typical of magnetic hyperthermia (40–45°C), the H_A and M_S values for spherical FeO/Fe_3O_4 MNPs are approximately 1.5 times lower

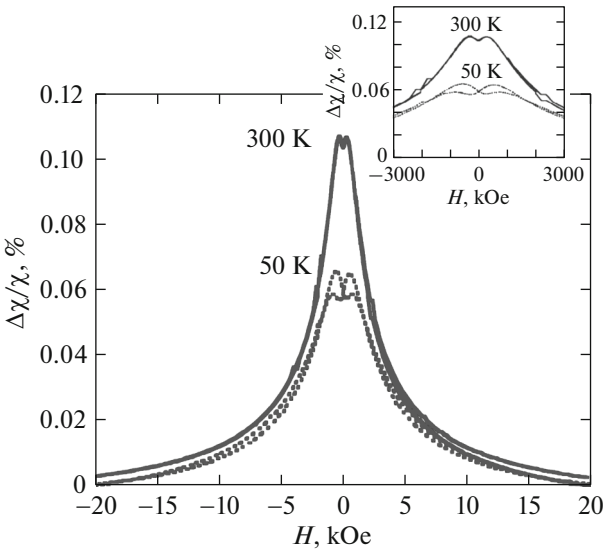

Fig. 3. Dependences of the transverse susceptibility of spherical FeO/Fe_3O_4 MNPs measured at 50 and 300 K.

and higher, respectively, than the corresponding values for cubic MNPs [6]. Therefore, these parameters affect the SAR of the studied MNPs differently. In order to verify this assumption, we have calculated the SAR for spherical FeO/Fe_3O_4 MNPs using the calorimetric method [6, 17]:

$$\mathrm{SAR} = \frac{m_s}{m_n} C_p \frac{\Delta T}{\Delta t}. \qquad (2)$$

Here, C_p is the specific heat capacity of the solution, m_s is the mass of the solution, m_n is the mass of nanoparticles, and $\Delta T/\Delta t$ is the initial slope of the heating temperature dependence shown in Fig. 4a. It can be seen that the heating rate increases gradually with the magnetic field strength. Thus, controlled variation of the external field strength is a simple path toward the target MNP interval of temperatures (40–44°C) that induce death of malignant cells, which are more sensitive to high temperatures, and leave normal cells unaffected [2, 4]. This becomes even more obvious when one compares the SAR values in Fig. 4b. It follows from the analysis of TS data that an enhancement of the effective anisotropy results in an increase in the SAR value even in exchange-coupled

Table 1. Magnetization, coercivity, and normalized remanent magnetization at 300 and 50 K of core–shell FeO/Fe_3O_4 nanoparticles of different shapes

Particle shape	H_C 50 K	H_C 300 K	M_S 50 K	M_S 300 K	M_r/M_S 50 K	M_r/M_S 100 K
Spheres	60	5	75	71	0.11	0
Cubes [6]	1050	60	45	48	0.21	0.05

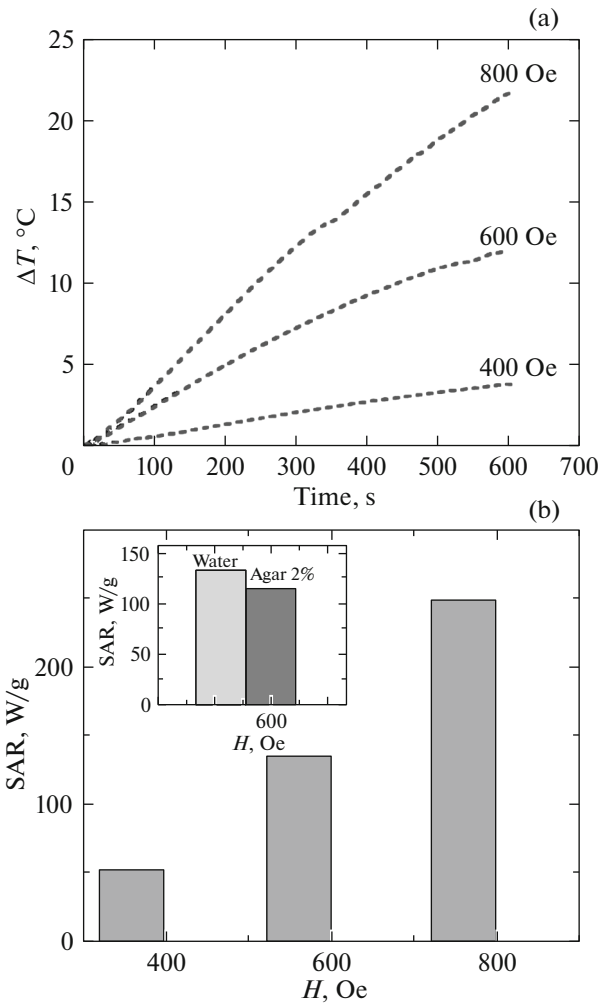

Fig. 4. (a) Dependences of the rate of heating of spherical FeO/Fe_3O_4 MNPs on the external magnetic field strength in the range of 400–800 Oe. (b) SAR values derived from the MNP heating curves. The SAR values obtained at 600 Oe for nanoparticles dispersed in water (left) and agar (right) are shown in the inset.

FeO/Fe_3O_4 MNPs with a lower saturation magnetization. This is indicative of the importance of magnetic anisotropy for magnetic hyperthermia. In order to simulate the real-world environment and determine the efficiency of MNP heating more accurately, FeO/Fe_3O_4 MNPs were dispersed in agar, where the increased viscosity restricts the physical rotation of particles. The SAR values for spherical FeO/Fe_3O_4 MNPs dispersed in water and in agar are shown in the inset in Fig. 4b. The SAR of spherical MNPs dispersed in agar is 10% higher than that of particles dispersed in water. This suggests that the contribution of physical rotation of MNPs to the heating efficiency is insignificant. A similar result was obtained for cubic FeO/Fe_3O_4 MNPs [6].

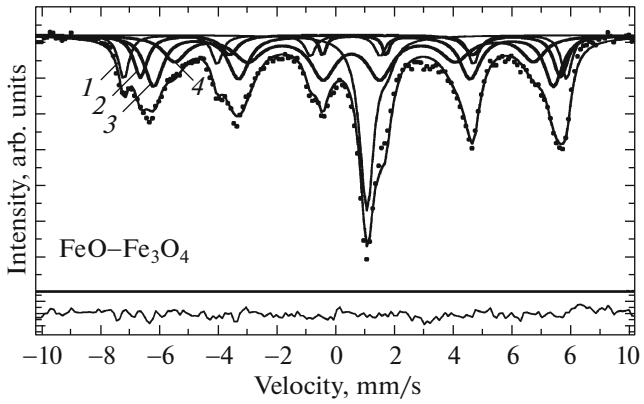

Fig. 5. Room-temperature Mössbauer spectrum of FeO/Fe_3O_4 MNPs. Dots represent experimental data, and the solid curve is the result of modeling. Zeeman splitting lines: (*1*) correspond to the maghemite (γ-Fe_2O_3) phase, (*2*) tetrahedral sites in the magnetite structure, (*3*) octahedral sites in the magnetite structure, and (*4*) iron ions located in interfacial regions and in the surface layer of particles. The residual is shown below the spectrum..

3.1. Mössbauer Studies of FeO/Fe_3O_4 MNPs

A powder of FeO/Fe_3O_4 MNPs prepared for Mössbauer studies was introduced into a special plastic container. The experimental Mössbauer spectrum of spherical FeO/Fe_3O_4 MNPs measured at room temperature without any external magnetic fields is shown in Fig. 5. The spectrum reveals complex magnetic interactions attributable to the presence of several magnetic phases in the studied FeO/Fe_3O_4 MNPs and their probable superparamagnetic behavior typical of small magnetic particles. It can be seen that the room-temperature Mössbauer spectrum of FeO/Fe_3O_4 MNPs contains a doublet with unresolved lines superimposed onto the lines of Zeeman sextuplets.

The MS of FeO/Fe_3O_4 MNPs were processed mathematically using MOSFIT [28] and a model featuring (1) a doublet located in the region of zero velocity (paramagnetic phase) and (2) four Zeeman sextuplets of iron oxides in the magnetically ordered state. Dots in Fig. 5 correspond to experimental data, and the solid curve is the resulting model spectrum. The hyperfine interaction (HFI) parameters determined by processing the experimental MS are presented in Table 2. These data suggest the following. The Zeeman splitting lines (*1* in Fig. 5) may be attributed to the maghemite γ-Fe_2O_3 phase at 296 K. The maghemite structure is the defect magnetite structure (cation-deficient spinel type). It was demonstrated in [31–34] that the MS of macroscopic particles contain Zeeman splitting lines that are transformed into relaxation spectra (an intense doublet is superimposed onto low-intensity Zeeman splitting lines) in the case of MNPs with a size of ~5 nm. However, the spectra in Fig. 5 reveal only the Zeeman sextuplet of maghemite and no

Table 2. Hyperfine interaction parameters for spherical core–shell FeO/Fe_3O_4 nanoparticles determined based on the experimental Mössbauer spectra (*K* is the spectrum component, Γ is the width of doublet lines, Γ_1 is the width of the outer lines of the Zeeman sextuplet, *IS* is the isomer shift relative to metallic iron, *QS* is the quadrupole splitting, H_{eff} is the effective magnetic field at the nuclei of iron ions, and *S* is the relative area of the spectrum component)

Doubles					
K	Γ, mm/s	*IS*, mm/s	*QS*, mm/s	*S*, %	
1	0.56 ± 0.11	1.37 ± 0.11	0.649 ± 0.11	17	
Sextets					
K	Γ_1, mm/s	*IS*, mm/s	*QS*, mm/s	H_{eff}, T	*S*, %
1	0.47 ± 0.04	0.29 ± 0.02	−0.01 ± 0.05	46.87 ± 0.10	10
2	0.64 ± 0.17	0.36 ± 0.025	−0.16 ± 0.05	45.01 ± 0.27	16
3	0.66 ± 0.10	0.62 ± 0.011	0.08 ± 0.02	42.97 ± 0.10	26
4	0.83 ± 0.09	0.53 ± 0.01	−0.03 ± 0.03	38.97 ± 0.18	31

relaxation phenomena. A similar pattern was observed for maghemite MNPs 15–20 nm in size at 295 K; the spectra were then approximated by a single sextet associated with ^{57}Fe nuclei attributed to Fe^{3+} ions [35, 36]. The effective magnetic fields in maghemite in FeO/Fe_3O_4 MNPs are weaker than those in maghemite macrocrystals; in addition, two nonequivalent positions of iron ions are observed in these macrocrystals. Such weakening of effective fields and the collapse of Zeeman sextuplets into a single one is observed in nanosized maghemite crystallites [33–36]. The following parameter values were derived from the experimental room-temperature MS of bulk magnetite: sextuplets with a smaller (compared to α-Fe) isomer shift δ = 0.25–0.31 mm/s and higher values of the effective hyperfine magnetic field H_{eff} = 487–495 kOe are attributed to ^{57}Fe nuclei at tetrahedral sites of magnetite, while sextuplets with larger isomer shifts δ = 0.61–0.68 mm/s and lower values of the effective hyperfine magnetic field H_{eff} = 458–462 kOe correspond to ^{57}Fe nuclei at octahedral sites. It follows from the comparison of HFI data for magnetite macrocrystals (see, e.g., [32, 37–40] with the values in Table 2 characterizing FeO/Fe_3O_4 MNPs that the sextuplet with a smaller isomer shift δ = 0.36 mm/s and higher H_{eff} = 450 kOe corresponds to ^{57}Fe nuclei at tetrahedral sites (*2* in Fig. 5) in the magnetite structure, while the sextuplet with a larger isomer shift δ = 0.62 mm/s and lower H_{eff} = 430 kOe corresponds to ^{57}Fe nuclei at octahedral sites (*3* in Fig. 5). The isomer shift for ^{57}Fe nuclei in a tetrahedral environment is typical of Fe^{3+} ions, while the isomer shift for ^{57}Fe nuclei in an octahedral environment is considerably larger and falls between the values characterizing Fe^{2+} and Fe^{3+}. The latter fact is attributable to the presence of Fe^{2+} and Fe^{3+} ions at octahedral sites. Electron transitions occur between these ions in the temperature interval of 115–120 K (Verwey transition T_V). The magnitudes of effective magnetic fields determined for FeO/Fe_3O_4 MNPs (Table 2) are significantly lower than those corresponding to magnetite macrocrystals. This is not surprising, since the weakening of effective fields in small magnetite particles was reported in [30, 37–39], and the studied MNPs are smaller than ~20 nm.

Zeeman sextuplet *4* (Fig. 5) may be attributed to iron ions located in interfacial regions and in the surface layer of particles. It should be noted that interfacial $Fe_xO/Fe_3O_4/\gamma\text{-}Fe_2O_3$ structures may be present in the studied MNPs. In addition to the paramagnetic wustite line in the region of zero velocity, the broad central part of the absorption spectrum may contain the lines of superparamagnetic contributions of magnetite, Fe_xO inclusions, and interfacial states manifesting relaxation effects. However, these contributions are small, and the Mössbauer effect for these states may be so weak as to make the absorption lines, which are much less intense than the spectral lines of magnetite and maghemite phases, indistinguishable.

The unresolved doublet lines (*5* in Fig. 5) in the region of zero velocity are typical of the spectra of wustite Fe_xO with a nonstoichiometric composition [11, 35, 36, 41–44]. The results of examination of $Fe_{1-x}O$ compounds of various compositions prepared from $\alpha\text{-}Fe_2O_3$ powders by annealing in inert atmospheres chosen so as to obtain the needed wustite composition were presented in [11, 41–44]. When annealed in an inert or oxidizing atmosphere, wustite MNPs transform into high-quality magnetite or maghemite nanocrystals (observed using X-ray diffraction, SAED, and SQUID). The aim of the studies reported in [11, 41–43] was to examine the capacity of chemical methods to control the size, the morphology, and, ultimately, the properties of iron oxides in the composition range from Fe_xO to Fe_2O_3 with a focus on Fe_xO nanoparticles used as the initial nanocrystal precursor to oxides in a higher oxidation state. It should be noted that the experimental MS presented in Fig. 5 are similar to the spectra of a mixture of

$Fe_{1.0}O$ and Fe_3O_4 at 297 K [11, 35, 44, 45]. However, what is important is that X-ray diffraction studies do not allow one to distinguish between magnetite and maghemite, while Mössbauer measurements provide an opportunity to detect these phases and identify them. No lines attributed to iron ions in the low-spin state Fe^{2+} were found in the MS.

The relative amounts of magnetite, maghemite, and wustite phases obtained based on the experimental absorption MS under the assumption of equal recoil-free fractions for these phases are given in Table 2.

Thus, the analysis of experimental MS of FeO/Fe_3O_4 MNPs (Fig. 5) clearly showed that these spectra contain a single sextet attributed to maghemite γ-Fe_2O_3, two sextets corresponding to iron oxide Fe_3O_4, and a doublet representing wustite FeO. This implies that three phases (magnetite, maghemite, and wustite) are simultaneously present in the studied FeO/Fe_3O_4 MNPs.

4. CONCLUSIONS

Magnetic spherical core–shell FeO/Fe_3O_4 nanoparticles were synthesized, and their properties were studied. The interaction between the antiferromagnetic Fe_3O_4 shell and ferrimagentic FeO induces exchange bias. It was demonstrated that the saturation magnetization and the effective anisotropy may be adjusted by varying the ratio of components and the morphology of FeO/Fe_3O_4 nanoparticles. This provides an opportunity to control the efficiency of heating of these nanoparticles. The potential to enhance the SAR of exchange-coupled magnetic nanoparticles by tuning their effective anisotropy, which is more convenient in the context of development of advanced biomedical materials, was demonstrated. The obtained XPS, XRD, and Mössbauer data and the results of magnetic measurements confirm that core–shell FeO/Fe_3O_4 MNPs are suitable for hyperthermic therapy. Mössbauer spectroscopy was used to analyze the phase composition of the synthesized MNPs. Mössbauer data revealed the simultaneous presence of three phases (magnetite Fe_3O_4, maghemite γ-Fe_2O_3, and wustite FeO) in the studied spherical core–shell FeO/Fe_3O_4 MNPs.

ACKNOWLEDGMENTS

A.A. Valiullin acknowledges partial support from the Competitiveness Enhancement Program of the Kazan Federal University.

REFERENCES

1. K. Hayashi, Y. Sato, W. Sakamoto, and T. Yogo, ACS Biomater. Sci. Eng. **3**, 95 (2017).
2. D. Ortega and Q. Pankhurst, in *Nanoscience. Nanostructures through Chemistry* (R. Soc. Chem., Cambridge, 2013), Vol. 1, p. 60.
3. Z. Ling-Yun, L. Jia-Yi, O. Wei-Wei, L. Dan-Ye, L. Li, L. Li-Ya, and T. Jin-Tian, Chin. Phys. B **22**, 108104 (2013).
4. P. Guardia, A. Riedinger, H. Kakwere, F. Gazeau, and T. Pellegrino, in *Bio- and Bioinspired Nanomaterials,* Ed. by D. Ruiz-Molina, F. Novio, and C. Roscini (Wiley-VCH, Weinheim, 2015), Pt. 6.
5. K. Chatterjee, S. Sarkar, K. J. Rao, and S. Paria, Adv. Colloid Interface Sci. **209**, 8 (2014).
6. H. Khurshid, J. Alonso, Z. Nemati, M. H. Phan, P. Mukherjee, M. L. Fdez-Gubieda, J. M. Barandiarán, and H. Srikanth, J. Appl. Phys. **117**, 17A337 (2015).
7. C. L. Dennis and R. Ivkov, Int. J. Hypertherm. **29**, 715 (2013).
8. N. A. Usov and B. Ya. Liubimov, J. Appl. Phys. **112**, 023901 (2012).
9. C. Martinez-Boubeta, K. Simeonidis, A. Makridis, M. Angelakeris, O. Iglesias, P. Guardia, A. Cabot, L. Yedra, S. Estrade, F. Peiro, Z. Saghi, P. Midgley, I. Conde-Leboran, D. Serantes, and D. Baldomir, Sci. Rep. **3**, 1652 (2013).
10. J. H. Lee, J. T. Jang, J. S. Choi, S. H. Moon, S. H. Noh, J. W. Kim, J. G. Kim, I. S. Kim, K. L. Park, and J. Cheon, Nat. Nanotechnol. **6**, 418 (2011).
11. F. X. Redl, C. T. Black, G. C. Papaefthymiou, R. L. Sandstrom, M. Yin, H. Zeng, C. B. Murray, and S. P. O'Brien, J. Am. Chem. Soc. **126**, 14583 (2004).
12. M. H. Phan, J. Alonso, H. Khurshid, P. Lampen-Kelley, S. Chandra, K. S. Repa, Z. Nemati, R. Das, Ó. Iglesias, and H. Srikanth, Nanomater. **6**, 221 (2016).
13. P. Poddar, T. Fried, and G. Markovich, Phys. Rev. B **65**, 172405 (2002).
14. E. Wetterskog, C. W. Tai, J. Grins, L. Bergstrom, and G. Salazar-Alvarez, ACS Nano **7**, 7132 (2013).
15. H. T. Hai, H. Kura, M. Takahashi, and T. Ogawa, J. Appl. Phys. **107**, 09E301 (2010).
16. M. I. Bodnarchuk, M. V. Kovalenko, H. Groiss, R. Resel, M. Reissner, G. Hesser, R. T. Lechner, W. Steiner, F. Schaffler, and W. Heiss, Small **5**, 2247 (2009).
17. D. Kavich, J. Dickerson, S. Mahajan, S. Hasan, and J.-H. Park, Phys. Rev. B **78**, 174414 (2008).
18. X. Sun, N. F. Huls, A. Sigdel, and S. Sun, Nano Lett. **12**, 246 (2012).
19. K. Haneda and A. H. Morrish, Solid State Commun. **22**, 779 (1977).
20. S. Disch, E. Wetterskog, R. P. Hermann, A. Wiedenmann, U. Vainio, G. Salazar-Alvarez, L. Bergström, and T. Brückel, New J. Phys. **14**, 013025 (2012).
21. B. Luigjes, S. M. C. Woudenberg, R. de Groot, J. D. Meeldijk, H. M. T. Galvis, K. P. de Jong, A. P. Philipse, and B. H. Erne, J. Phys. Chem. C **115**, 14598 (2011).
22. M. Levy, A. Quarta, A. Espinosa, A. Figuerola, C. Wilhelm, M. García-Hernández, A. Genovese, A. Falqui, D. Alloyeau, R. Buonsanti, P. D. Cozzoli, M. A. Gar-

cía, F. Gazeau, and T. Pellegrino, Chem. Mater. **23**, 4170 (2011).

23. D. Amara, J. Grinblat, and S. Margerl, Mater. Chem. **22**, 2188 (2012).
24. G. F. Goya, T. S. Berquó, F. C. Fonseca, and M. P. Morales, J. Appl. Phys. **94**, 3520 (2003).
25. Y. Tai, L. Wang, G. Yan, J. M. Gao, H. Yu, and L. Zhang, Polym. Int. **60**, 976 (2011).
26. H. Khurshid, W. Li, S. Chandra, M. H. Phan, G. C. Hadjipanayis, P. Mukherjee, and H. Srikanth, Nanoscale **5**, 7942 (2013).
27. J. Vonhoene, R. G. Charles, and W. M. Hickam, J. Phys. Chem. **62**, 1098 (1958).
28. V. G. Semenov and V. Panchuk, MOSFIT - Software for Mössbauer Spectra Processing, private communication.
29. R. W. Cheary and A. A. Coelho, in *CCP14 Powder Diffraction Library* (Eng. Phys. Sci. Res. Council, Daresbury Laboratory, Warrington, UK, 1996).
30. *Nanoparticles Featuring Electromagnetic Properties, Science to Engineering* (Research Signpost, Kerala, India, 2012), p. 167.
31. I. N. Zakharova, M. A. Shipilin, V. P. Alekseev, and A. M. Shipilin, Tech. Phys. Lett. **38**, 55 (2012).
32. I. Diamandrescu, D. Mihaila-Tarabasanu, V. Teodorescu, and N. Popescu-Pogrion, Mater. Lett. **37**, 340 (1998).
33. J. A. Ramos Guivar, A. Bustamante, J. Flores, M. Mejía Santillan, A. M. Osorio, A. I. Martínez, L. de los Santos Valladares, and C. H. W. Barnes, Hyperfine Interact. **224**, 89 (2014).
34. S. Kubuki, Y. Watanabe, K. Akiyama, M. Ristić, S. Krehula, Z. Homonnay, E. Kuzmann, and T. Nishida, AIP Conf. Proc. **1622**, 134 (2014).
35. M. Fujinami and Y. Ujihira, J. Mater. Sci. **20**, 1859 (1985).
36. K. Kluchova, R. Zboril, J. Tucek, M. Pecova, L. Zajoncova, I. Safarik, M. Mashlan, I. Markova, D. Jancik, M. Sebela, H. Bartonkova, V. Belessi, P. Novak, and D. Petridis, Biomaterials **30**, 2855 (2009).
37. D. F. Gorozhankin, A. A. Eliseev, K. S. Napol'skii, A. V. Lukashin, A. V. Knot'ko, Yu. V. Maksimov, I. P. Suzdalev, P. Goernert, and Yu. D. Tret'yakov, Dokl. Chem. **396**, 132 (2004).
38. I. Deźsi, Cs. Fetzer, Á. Gombkoötö, I. Szücs, J. Gubicza, and T. Ungár, J. Appl. Phys. **103**, 104312 (2008).
39. H. Topsøe, J. A. Dumesic, and M. Boudart, J. Phys. **35** (12), C6-411 (1974).
40. H. P. Weber and S. S. Hafner, Zeitschr. Kristallogr. **133**, 327 (1971).
41. J. C. Park, D. Kim, C. S. Lee, and D. K. Kim, Bull. Korean Chem. Soc. **20**, 1005 (1999).
42. H. U. Hrynkiewic, D. S. Kulgawczuk, E. S. Mazanek, A. M. Pustowka, K. Tomala, and M. E. Wyderko, Phys. Status Solidi A **9**, 611 (1972).
43. C. A. McCammon and D. C. Price, Phys. Chem. Miner. **11**, 250 (1985).
44. L. F. Checherskaya, V. P. Romanov, and P. A. Tatsienko, Phys. Status Solidi A **2**, K177 (1973).
45. A. Glaria, M. L. Kahn, P. Lecante, B. Barbara, and B. Chaudret, Chem. Phys. Chem. **9**, 776 (2008).

Translated by D. Safin